Supplemental Material for "Microscopic origin of frictional rheology in dense suspensions: correlations in force space"

Jetin E. Thomas,[1,*] Kabir Ramola,[1,†] Abhinendra Singh,[2,‡]
Romain Mari,[3,§] Jeffrey Morris,[2,4,¶] and Bulbul Chakraborty[1,**]

[1]*Martin Fisher School of Physics, Brandeis University, Waltham, MA 02454, USA*
[2]*Benjamin Levich Institute, CUNY City College of New York, New York, NY 10031, USA*
[3]*Univ. Grenoble Alpes, CNRS, LIPhy, 38000 Grenoble, France*
[4]*Department of Chemical Engineering, CUNY City College of New York, New York, NY 10031*

(Dated: July 26, 2018)

In this document we provide supplemental figures and details of the calculations presented in the main text.

Macroscopic Friction Coefficient and DST Rheology

The existing mean-field theory of DST extends the suspension rheology framework [1] through the introduction of a stress- and ϕ-dependent microstructure parameter: the fraction of frictional contacts [2, 3]. The suspension rheology model embodies a constitutive relation: $\mu(\phi, I_v)$, where the viscous number $I_v \equiv \frac{\eta_f \dot{\gamma}}{P}$. In this framework, the shear viscosity of the suspension [1] is: $\eta = \frac{\mu(I_v(\phi))}{I_v(\phi)}$, and $I_v(\phi) \propto (\phi_m - \phi)^2$, where ϕ_m is the jamming packing fraction at which η diverges. In the jamming limit, $I_v \to 0$, one can also write a relationship between μ and I_v (Eq. 5 in Ref. [1]): $\mu - \mu_c \simeq I_v^{1/2}$, where, μ_c is a material parameter [1]. Using this, an equivalent expression for the viscosity is: $\eta \propto \mu(\mu - \mu_c)^{-2}$, which focuses on the divergence of the viscosity of frictional suspensions as $\mu \to \mu_c^+$. This is a consistent picture of the rate-independent, quasi-Newtonian rheology for a given microscopic friction coefficient.

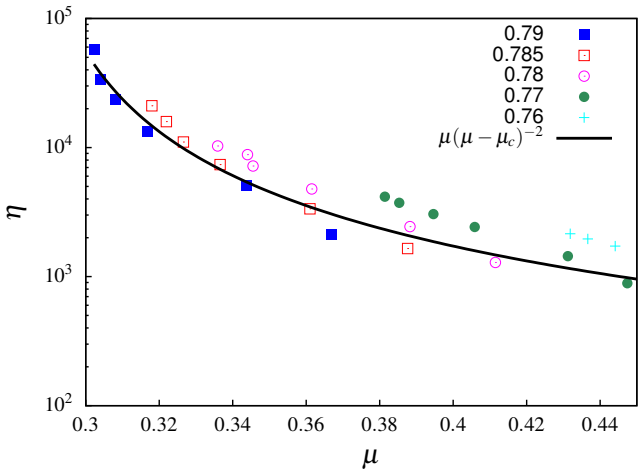

FIG. 1: (Color online) Plot of the viscosity, $\eta(\phi, \sigma_{xy})$ vs $\mu(\phi, \sigma_{xy})$ for different packing fractions, obtained from the simulations (symbols) compared to the constitutive relation: Eq. (1). Here $\mu_c = 0.285$, is chosen to be the lowest value of the stress anisotropy observed in the simulations. The viscosity η is measured in units of η_0, the viscosity of the underlying Newtonian fluid, and in our simulations we set $\eta_0 = 1$.

Below, we extend this theory of rate-independent, quasi-Newtonian rheology to dense suspensions. The physical picture underpinning the theory is the same as the mean-field theory of DST [2, 3]: frictional contacts increase with increasing imposed shear stress. In our theory, the effect of this increase is represented by the "order parameter" $\mu(\phi, \sigma_{xy})$. The theory for this order parameter is based on an effective pair potential in force space, as described in the main text. We propose that the viscosity has the same functional dependence on μ as in the rate-independent suspension rheology but the physics of thickening suspensions is encapsulated in the order parameter, $\mu(\phi, \sigma_{xy})$. The viscosity of a thickening suspension should diverge as $\phi \to \phi_m^-$, the jamming packing fraction of the frictional fluid [1–3], in the limit of $\sigma_{xy} \to \infty$ where the fraction of frictional contacts approaches unity. Therefore, we define $\mu_c = \mu(\phi = 0.80, \sigma_{xy} = 100\sigma_0)$, the value we obtain from the theory at the highest packing fraction and shear stress.

Thus:

$$\eta(\phi,\sigma_{xy}) \propto \mu(\phi,\sigma_{xy})\left(\mu(\phi,\sigma_{xy})-\mu_c\right)^{-2} \ . \tag{1}$$

The above constitutive relation is expected to be valid only close to μ_c, and as it is approached from above. In Fig. 1, we show that the increase in $\eta(\phi,\sigma_{xy})$ is primarily controlled by the decrease in $\mu(\phi,\sigma_{xy})$, close to μ_c. The functional form given in Eq. (1) is also seen to provide a good description of this correlation for the larger values of ϕ. We, therefore, use Eq. (1) to infer the rheological properties and compute the DST diagram. The difference with the Wyart-Cates theory is that we encapsulate the information about the microstructure in $\mu(\phi,\sigma_{xy})$ rather than in the fraction of frictional contacts [2, 3].

Simulating Dense Suspensions

We simulate a two-dimensional or monolayer suspension of non-Brownian spherical particles immersed in a Newtonian fluid under an imposed shear stress σ_{xy}. This gives rise to a velocity field $\vec{v} = \dot{\gamma}(t)\hat{\vec{v}}(\vec{x}) = \dot{\gamma}(t)(x_2,0)$ [4], with a time-dependent shear rate $\dot{\gamma}$ [5]. All our results are obtained with $N = 2000$ particles in a unit cell with Lees-Edwards boundary conditions. Bidispersity at a radii ratio of a and $1.4a$ and volume ratio of $1:1$ is used to avoid crystallization during flow [6]. In this simulation scheme, the particles interact through near-field hydrodynamic interactions (lubrication), a short-ranged repulsive force and frictional contact forces.

The motion is considered to be inertialess, so that the equation of motion reduces to a force balance between hydrodynamic ($\vec{F}_{\rm H}$), repulsive ($\vec{F}_{\rm R}$), and contact ($\vec{F}_{\rm C}$) forces:

$$0 = \vec{F}_{\rm H}(\vec{X},\vec{U}) + \vec{F}_{\rm C}(\vec{X}) + \vec{F}_{\rm R}(\vec{X}), \tag{2}$$

where $\vec{X}$ and $\vec{U}$ denote particle positions and their velocities/angular velocities respectively.

The translational velocities and rotation rates are made dimensionless with $\dot{\gamma}a$ and $\dot{\gamma}$, respectively. The hydrodynamic forces are the sum of a drag due to the motion relative to the surrounding fluid and a resistance to the deformation imposed by the flow:

$$\vec{F}_{\rm H}(\vec{X},\vec{U}) = -\overleftrightarrow{R}_{\rm FU}(\vec{X})\cdot\left(\vec{U}-\dot{\gamma}\hat{\vec{U}}^{\infty}\right) + \dot{\gamma}\overleftrightarrow{R}_{\rm FE}(\vec{X}) : \hat{\overleftrightarrow{E}}, \tag{3}$$

with $\hat{\vec{U}}^{\infty} = (\hat{\vec{v}}(y_1),\ldots,\hat{\vec{v}}(y_N),\hat{\vec{\omega}}(y_1),\ldots,\hat{\vec{\omega}}(y_N))$ and $\hat{\overleftrightarrow{E}} = (\hat{\overleftrightarrow{e}}(y_1),\ldots,\hat{\overleftrightarrow{e}}(y_N))$.

Details about the position-dependent resistance tensors $\overleftrightarrow{R}_{\rm FU}$ and $\overleftrightarrow{R}_{\rm FE}$ are available in [6]. We regularize the resistance matrix by introducing a small cutoff length scale $\delta = 10^{-3}$ [6].

We take a stablizing repulsive force which decays exponentially with the interparticle gap h as $|\vec{F}_R| = F_0\exp(-h/\lambda)$, with a characteristic length λ. This provides a simple model of screened electrostatic interactions which can often be found in aqueous systems [6–8], in which case λ is the Debye length. In the simulations, we set $\lambda = 0.02a$.

We model contact forces using linear springs and dashpots, a model that is commonly used in soft-sphere DEM simulations [9, 10]; the spring constants used here have a ratio $k_{\rm t} = 0.5k_{\rm n}$. For each applied stress, we adjust the spring stiffnesses such that the maximum particle overlaps do not exceed 3% of the particle radius in order to stay close to the rigid limit [6, 11]. The normal and tangential components of the contact force $\vec{F}_C^{(ij)}$ fulfill Coulomb's friction law $|F_{C,t}^{(ij)}| \le \mu_f |F_{C,n}^{(ij)}|$, where μ_f is the interparticle friction coefficient. In this study we use $\mu_f = 1.0$.

The unit scales for strain rate and stress are $\dot{\gamma}_0 \equiv F_0/6\pi\eta_0 a^2$ and $\sigma_0 \equiv \eta_0\dot{\gamma}_0 = \frac{F_0}{6\pi a^2}$, respectively, where η_0 is the viscosity of the underlying Newtonian fluid, and in our simulations we set $\eta_0 = 1$.

Based on the simulation results presented here and the model proposed in [2, 12], a phase diagram in (σ,ϕ) plane is displayed in Fig. 2. For low packing fraction $\phi < \phi_{\rm DST}$, CST is observed. For packing fractions, $\phi_{\rm DST} \le \phi < \phi_{\rm J}^{\mu}$, DST is observed between two flowing states. In this range of ϕ, red curve shows locus of DST points, i.e., $\frac{d\dot{\gamma}}{d\sigma_{xy}} = 0$. For $\phi > \phi_{\rm J}^{\mu}$, DST is observed between a flowing and solid–like shear jammed state. The stress required to observe DST as well as shear jamming decreases with increase in packing fraction and both eventually vanish on the approach to the isotropic jamming point.

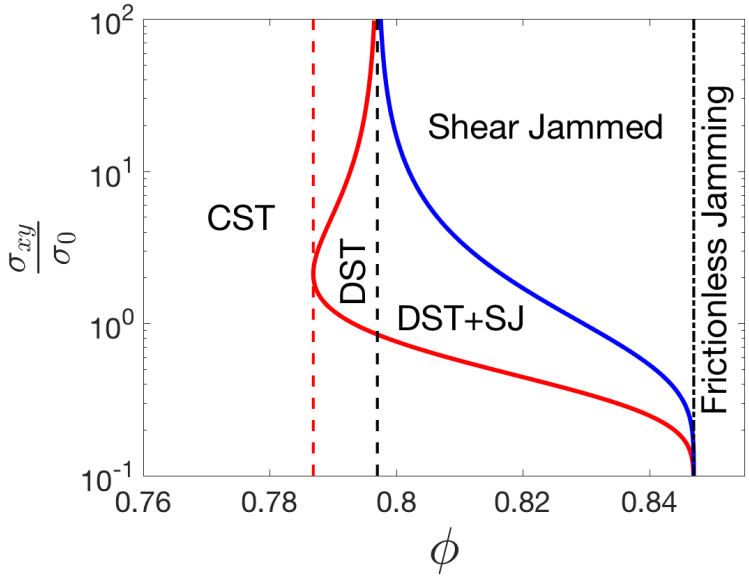

FIG. 2: (Color online) Phase diagram in the shear stress–packing fraction (σ_{xy}, ϕ) plane. The left (red) curve locates the points where $\frac{d\dot{\gamma}}{d\sigma_{xy}} = 0$. The right (blue) curve shows packing fraction dependent maximal stress above which the suspension is shear-jammed, i.e., above which no flowing states exist. Dashed and dotted-dashed black lines represent frictional and frictionless jamming points, respectively. The red dashed line shows the minimum packing fraction $\phi_{\rm DST}$ at which DST is observed. The regime of stress over which the viscosity scales as σ, defines the DST region.

Dimensions of the Force Tiling Box

Keeping the shear stress, $\sigma_{xy} = \sigma_{yx}$ and the real space dimensions, $L_x = L_y = L$ fixed implies that we fix

$$\Gamma_{\rm yy} = -\Gamma_{\rm xx} = \sigma \ . \tag{4}$$

We define

$$\mathcal{N}_1 = \Gamma_{\rm yx} + \Gamma_{\rm xy}, \tag{5}$$

and

$$\mathcal{P} = \Gamma_{\rm yx} - \Gamma_{\rm xy}. \tag{6}$$

The behaviour of these two quantities as ϕ and σ_{xy} are varied are shown in Figs. 3 and 4. In addition, we plot the density of vertices $\rho_v = N_v/A$, where N_v is the number of vertices, and $A = \left|\vec{\Gamma}_x \times \vec{\Gamma}_y\right|$ is the area of the force tiling box, as ϕ and σ_{xy} are varied in Fig. 5.

Constraints on the Stress and Force Moment Tensors

From Eq. (1) in the main text, the stress tensor $\overleftrightarrow{\sigma}$ is given by

$$\overleftrightarrow{\sigma} = \begin{pmatrix} \sigma_{xx} & \sigma_{xy} \\ \sigma_{yx} & \sigma_{yy} \end{pmatrix} = \frac{1}{L^2}\overleftrightarrow{\Sigma} = \frac{1}{L^2}\begin{pmatrix} \Sigma_{xx} & \Sigma_{xy} \\ \Sigma_{yx} & \Sigma_{yy} \end{pmatrix} = \frac{1}{L}\begin{pmatrix} \Gamma_{\rm yx} & \Gamma_{\rm yy} \\ -\Gamma_{\rm xx} & -\Gamma_{\rm xy} \end{pmatrix}. \tag{7}$$

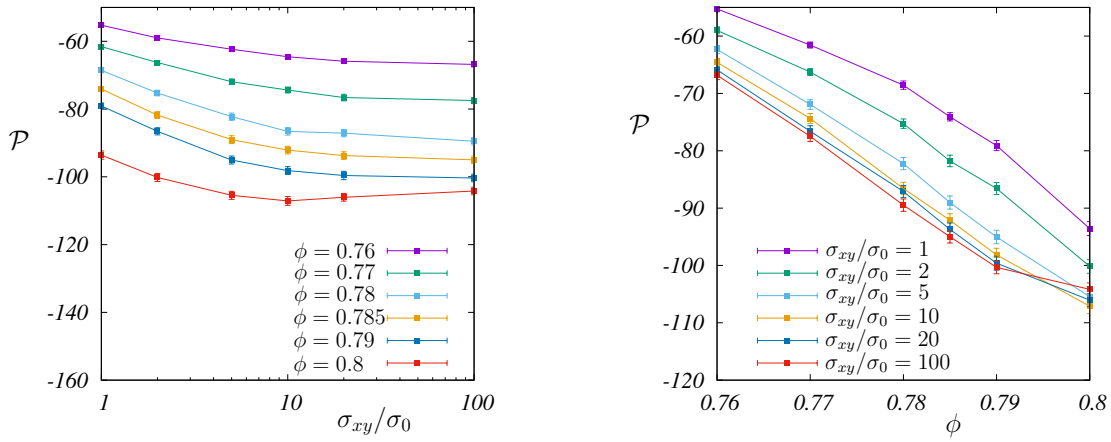

FIG. 3: (Color online) Observed $\mathcal{P}$ from the data.

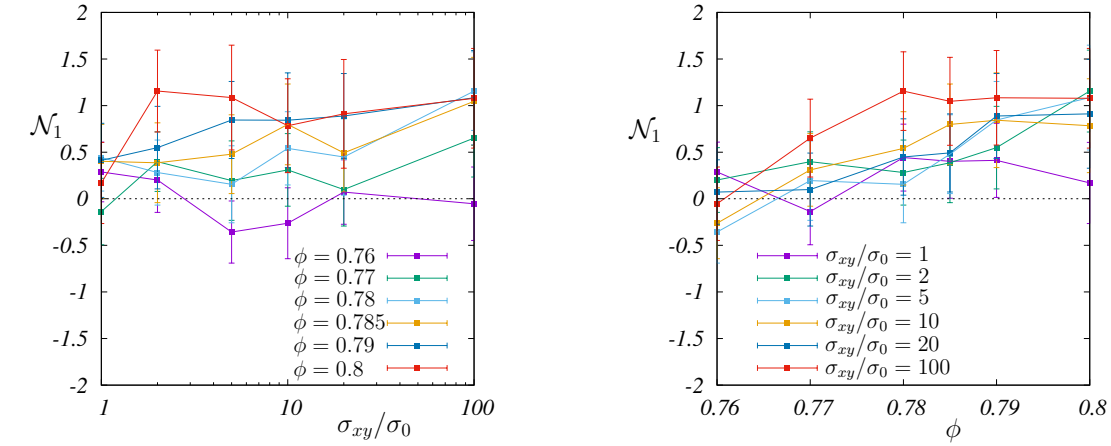

FIG. 4: (Color online) Observed $\mathcal{N}_1$ from the data.

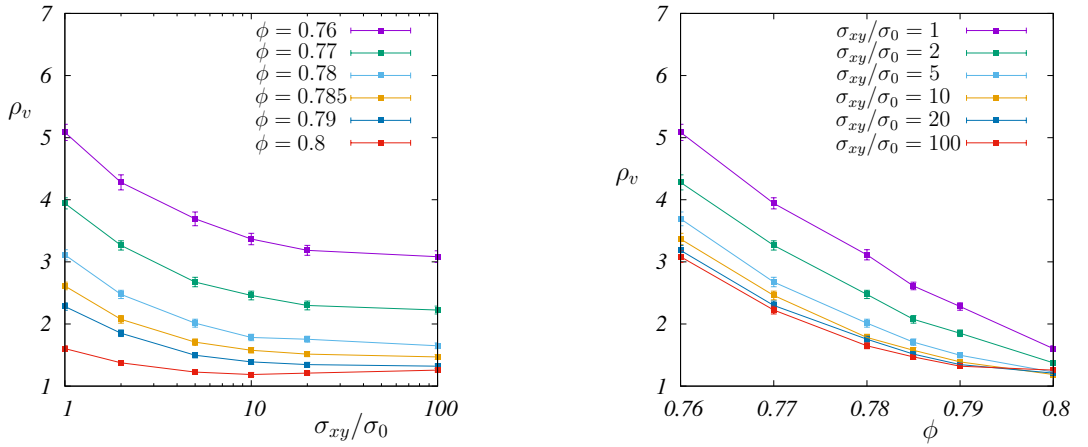

FIG. 5: (Color online) Observed density of vertices in the force tiling, $\rho_v = N_v/A$ from the data.

Global torque balance implies $\overleftrightarrow{\sigma}^T = \overleftrightarrow{\sigma}$, hence $\sigma_{xy} = \sigma_{yx}$. The eigenvalues of $\overleftrightarrow{\sigma}$ are then given by

$$\lambda_\pm = \frac{1}{2}\left((\sigma_{xx}+\sigma_{yy}) \pm \sqrt{(\sigma_{xx}-\sigma_{yy})^2 + 4\sigma_{xy}^2}\right) \tag{8}$$

$$= \frac{1}{2L^2}\left((\Sigma_{xx}+\Sigma_{yy}) \pm \sqrt{(\Sigma_{xx}-\Sigma_{yy})^2 + 4\Sigma_{xy}^2}\right). \tag{9}$$

The normal stress difference is given by

$$N_1 = \sigma_{xx} - \sigma_{yy} = \frac{1}{L^2}(\Sigma_{xx} - \Sigma_{yy}) = \frac{1}{L^2}\tilde{N}_1. \tag{10}$$

Using Eq. (5) we have

$$\tilde{N}_1 = L(\Gamma_{\mathrm{yx}} + \Gamma_{\mathrm{xy}}) = L\mathcal{N}_1. \tag{11}$$

The difference in the eigenvalues of the stress tensor is given by

$$\tau = \frac{1}{L^2}\sqrt{(\tilde{N}_1)^2 + 4\Sigma_{xy}^2} = \frac{1}{L}\sqrt{(\mathcal{N}_1)^2 + 4\sigma^2}, \tag{12}$$

where we have used Eqs. (4) and (5) in the last equality. The sum of the eigenvalues is given by

$$2P = \sigma_{xx} + \sigma_{yy} = \frac{1}{L^2}(\Sigma_{xx} + \Sigma_{yy}) = \frac{\mathcal{P}}{L}, \tag{13}$$

where P is the pressure, and we have used Eq. (6) in the last equality. The stress anisotropy, defined as the ratio of the difference of the eigenvalues (τ) to the sum of the eigenvalues ($2P$) of the stress tensor can then be expressed as

$$\frac{\tau}{2P} = \frac{\sqrt{\left(\tilde{N}_1\right)^2 + 4\Sigma_{xy}^2}}{\Sigma_{xx}+\Sigma_{yy}} = \frac{\sqrt{(\mathcal{N}_1)^2 + 4\sigma^2}}{\mathcal{P}}, \tag{14}$$

which is Eq. (2) in the main text. Since $\mathcal{N}_1/\mathcal{P}$ is observed to be small (Figs. 3 and 4), the stress anisotropy is

$$\frac{\tau}{2P} \approx \frac{2\sigma}{\mathcal{P}} = \frac{\sigma_{xy}}{P} = \mu. \tag{15}$$

The behaviour of μ observed from the simulations as ϕ and σ_{xy} are varied is shown in Fig. 6. Finally, if we set $\mathcal{N}_1 = 0$, the area of the bounding box of the force tiles is given by

$$A = \left|\vec{\Gamma}_x \times \vec{\Gamma}_y\right| = \Gamma_{\mathrm{xx}}\Gamma_{\mathrm{yy}} - \Gamma_{\mathrm{xy}}\Gamma_{\mathrm{yx}} = \sigma^2\left(\frac{1}{\mu^2} - 1\right). \tag{16}$$

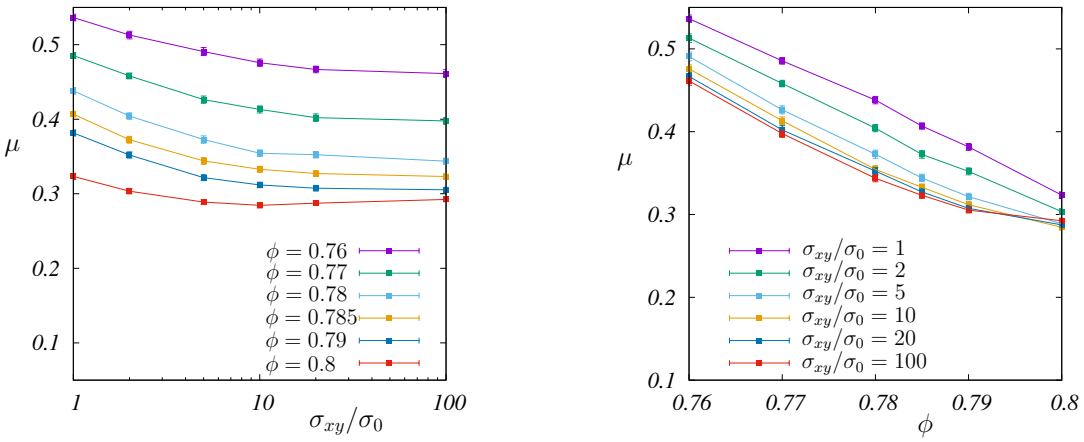

FIG. 6: (Color online) Observed stress anisotropy μ from the simulation of suspensions. The values of μ calculated from the theory (Fig. 4 in the main text) are in semiquantitative agreement with these results. However, the simulations show a larger range of variation.

Clustering in Force Space

As observed from the pair correlation functions in height space (Fig. 2 in the main text), there is a clustering of the height vertices as the shear stress is increased. To quantify this behaviour we analyze the radially averaged correlation function

$$g_2(h) = \frac{1}{2\pi h} \int d^2\vec{h}\; g_2(\vec{h})\; \delta\left(h - |\vec{h}|\right). \tag{17}$$

This radial correlation function is fit well at small force scales by the following form

$$g_2(h) = 1 + \mathrm{C}\left(\exp\left(\frac{1}{a + bh^2}\right) - 1\right). \tag{18}$$

As an example, we plot the fit using this form for $\phi = 0.76$ and $\sigma_{xy} = 10\sigma_0$ in Fig. 7, showing that this form captures the behaviour at small force scales accurately.

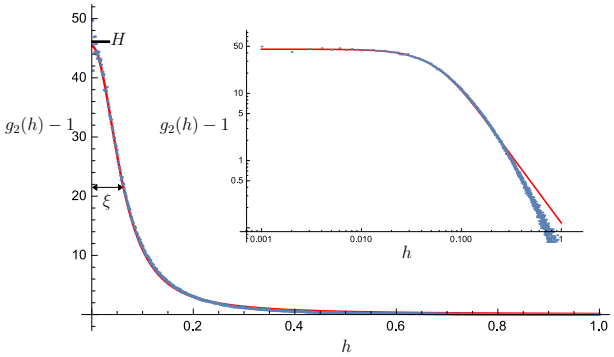

FIG. 7: (Color online) Comparison of $g_2(h)$ for $\phi = 0.76$, $\sigma_{xy} = 10\sigma_0$ (dots), and the fit (solid line) using the form given in Eq. (18), with $C = 5.17576, a = 0.438877$ and $b = 43.8752$. (Inset) the same data in a log-log plot.

Using this fit, we compute three quantities that provide information about the clustering at small force scales, We compute

- The peak height H, given by

$$H = g_2(0) - 1 = C\left(e^{\frac{1}{a}} - 1\right). \tag{19}$$

- The clustering length scale ξ defined as the full width at half maximum of $g_2(h)$, given by

$$\xi = \frac{\sqrt{1 - a\log\left(\frac{1}{2}\left(e^{\frac{1}{a}} + 1\right)\right)}}{\sqrt{b\log\left(\frac{1}{2}\left(e^{\frac{1}{a}} + 1\right)\right)}}. \tag{20}$$

  In the theory developed in the main text, we do not consider the region within ξ, which corresponds to very small forces in our statistical mechanics model.

- The clustering intensity defined as the area

$$\mathcal{I} = \int_0^{\xi} g_2(h)dh. \tag{21}$$

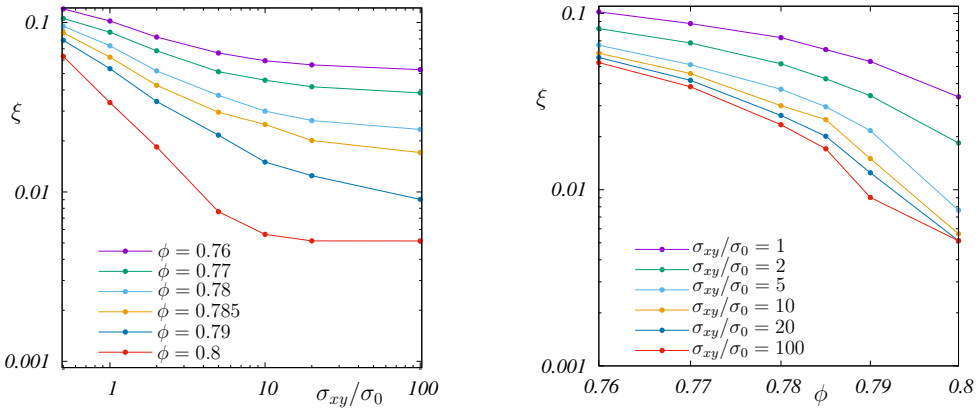

FIG. 8: (Color online) Observed clustering length scale ξ from the data. These are much smaller than the scales relevant in the effective theory discussed in the main text, where the typical force scales are ~ 1.

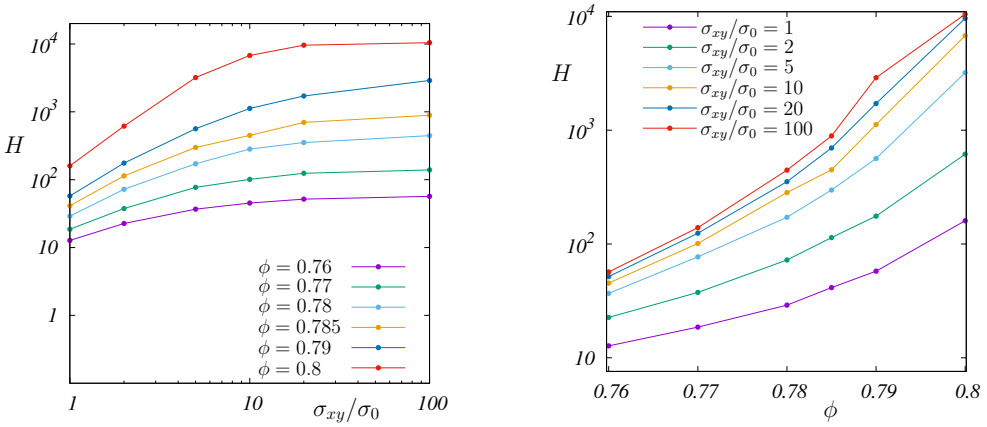

FIG. 9: (Color online) Observed height H, of the peak in $g_2(h)$.

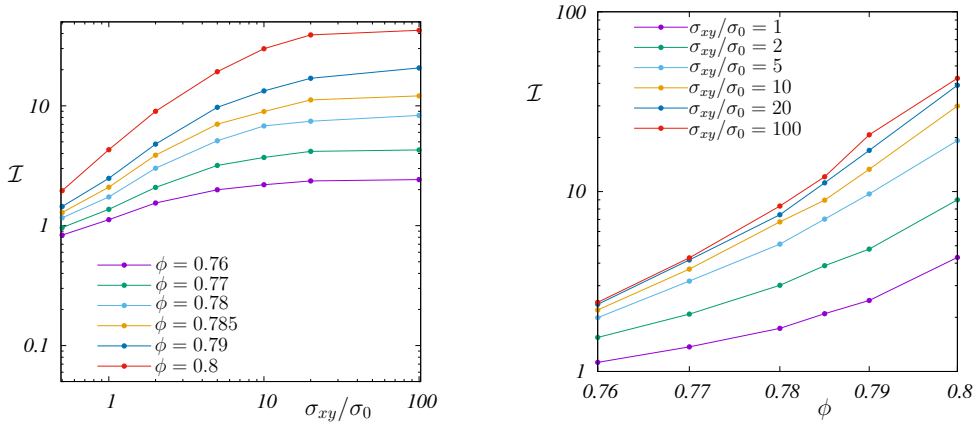

FIG. 10: (Color online) Observed clustering intensity $\mathcal{I}$ from the data.

Rotation of Pair Correlation Patterns

As shown in the main text, the "lobes" of $g_2(h_x, h_y)$ representing regions where the correlations are higher than that of an ideal gas, rotate as ϕ is increased. We quantify this rotation by analyzing the lobes in $g_2(h_x, h_y)$. As an example the Pair Correlation Function of Vertices (PCFV) for $\phi = 0.77$ and $\sigma_{xy} = 1\sigma_0$ is shown in Fig. 11. This displays a characteristic "butterfly" pattern, with four lobes. The angles θ_1 and θ_2, defined in Fig. 11, show a clear evolution with both ϕ and σ_{xy}, as shown in Fig. 12.

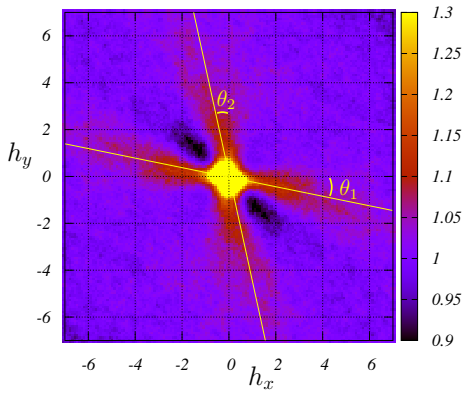

FIG. 11: (Color online) Observed Pair Correlation Function of Vertices (PCFV) $g_2(\vec{h})$ at $\phi = 0.77, \sigma_{xy} = 1\sigma_0$. We use the angles θ_1 and θ_2 to quantify the change in anisotropy as ϕ and σ_{xy} are varied.

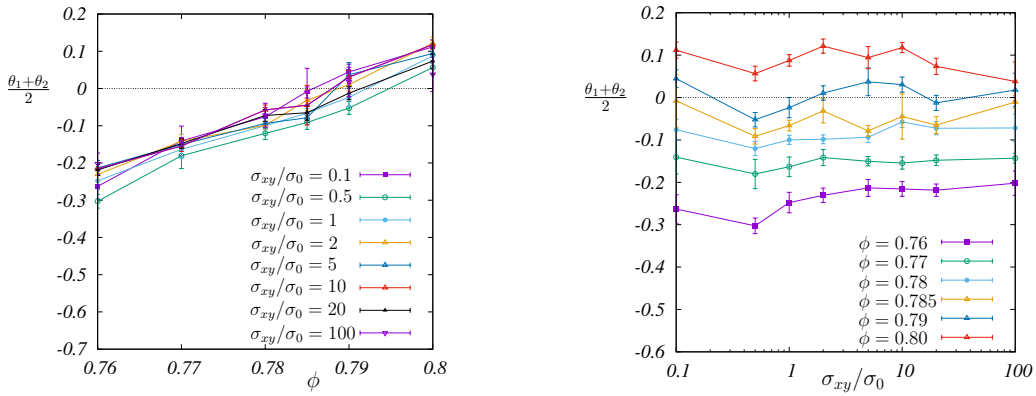

FIG. 12: (Color online) Observed rotation in the lobes (defined in Fig. 11) of the Pair Correlation Function of Vertices (PCFV) $g_2(\vec{h})$.

Results for Viscosity

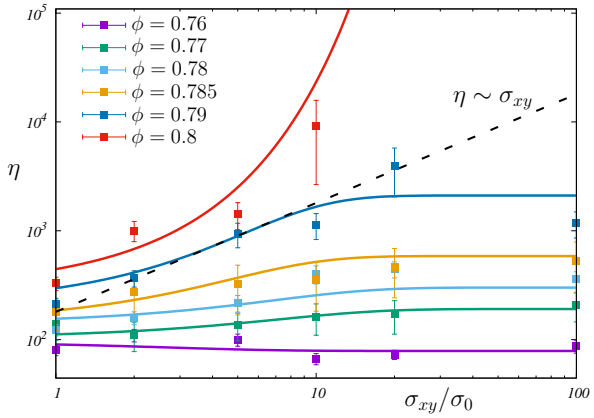

FIG. 13: (Color online) Viscosity (η) as a function of the imposed shear stresses (σ_{xy}), computed using Eq. (1), at different packing fractions (ϕ). The points at which $\eta \sim \sigma_{xy}$ (dashed line) define the limits of the DST regime.

Monte Carlo Sampling of the Energy function

We treat the system using the NPT ensemble [13], allowing for fluctuations in box shape [14]. We fix $\Gamma_{yy} = -\Gamma_{xx} = \sigma = 15$ as observed from the data. We also fix the magnitude of Γ_{xy} and Γ_{yx} to be equal, since $N_1 \approx 0$ as observed from simulations (see Fig. 4). The shape, and the area, of the force tiling is then determined by a single shape parameter μ.

While performing Monte Carlo simulations of the interacting gas of height vertices, it becomes necessary to avoid clustering of the vertices as the density is increased. Therefore in addition to the potential given in Eq. (5) in the main text, we add a very short ranged "hard-core" potential that prevents vertices from approaching very close to each other. We choose this hard-core potential to be a smoothly varying function of the form

$$V_{2,HC}(\vec{h}) = \exp((h_{HC}/|h|)^2) - 1, \tag{22}$$

where we choose $h_{HC} = 0.02$, much smaller than the intermediate force scales ≈ 1 which is the focus of our study. Finally, in order to avoid long-range effects which are sensitive to numerical error induced by the low statistics of $g_2(\vec{h})$ at large force scales, we cut off the potential at a distance beyond which the anisotropy becomes unimportant. This is done by multiplying the potential with a Fermi function that falls off sharply at a distance $h_{CO} = 10$. We have

$$V_{\phi,\sigma}(\vec{h}) = \frac{1}{1 + \exp\left(3(|h| - h_{CO})\right)} \left(V_2(\vec{h}) + V_{2,HC}(\vec{h})\right), \tag{23}$$

Finally we use this potential $V_{\phi,\sigma}(\vec{h})$ to perform Monte Carlo simulations of the interacting gas of vertices using the Metropolis algorithm (and $\beta = 1$). The displacement of each vertex is chosen from a Gaussian distribution with variance 10^{-4}, and periodic boundary conditions are imposed using the dimensions of the force tiling box $(\vec{\Gamma}_x, \vec{\Gamma}_y)$. We also perform changes to the dimensions of the force tiling box, with the vertices being transformed affinely with every global change of the box shape. We attempt a change in the dimensions of the box at every tenth Monte Carlo step, with weights chosen using the energy

$$E \equiv \sum_{i \neq j} V_{\phi,\sigma}(\vec{h}_i - \vec{h}_j) + N_v f_p^* A. \tag{24}$$

We use these simulations to verify that the pair correlations generated using these potentials match the original $g_2(\vec{h})$ obtained from the NESS of simulated suspensions (as shown in Fig. 2 of the main text).

Next, in order to compute the "free energy" function $\mathcal{F}_{\mu;\phi,\sigma}$ of the system, we sample the "energy" function $\epsilon_{\phi,\sigma}(\mu, N_v)$ given in Eq. (6) in the main text. We perform this sampling as follows. For every realization of the system at a different μ (which defines the shape and the size of the confining box), we make the affine transformation

$$\begin{pmatrix} h_x \\ h_y \end{pmatrix} = \begin{pmatrix} \Gamma_{xx} & \Gamma_{xy} \\ \Gamma_{yx} & \Gamma_{yy} \end{pmatrix} \begin{pmatrix} s_x \\ s_y \end{pmatrix}, \tag{25}$$

where the positions $\vec{s}_i$ are now confined to be within a 1×1 box. In terms of the scaled coordinates $\{\vec{s}_i\}$, we have

$$\exp(-\epsilon_{\phi,\sigma}(\mu, N_v)) = \int_{1\times 1} \prod_{i=1}^{N_v} d\vec{s}_i \exp\left(-\sum_{i,j} \tilde{V}_{\phi,\sigma}(\vec{s}_i - \vec{s}_j)\right), \tag{26}$$

where $\tilde{V}$ is now the affinely transformed potential. We perform a Monte Carlo (MC) sampling to obtain $\epsilon_{\phi,\sigma}(\mu, N_v)$ for different values of the number of vertices $N_v = 128, 256, 512, 768$ and 1024.

For a fixed μ, we create an ensemble of configurations $C_n \equiv \{\vec{s}_i^n\}$ with $n = 1, 2...N_{MC}$ with positions chosen uniformly within the 1×1 box. The computational cost of arranging N_v points in the box and computing $\left(\sum_{i,j} \tilde{V}_{\phi,\sigma}(\vec{s}_i^n - \vec{s}_j^n)\right)$ for each configuration is $O(N_v^2)$. For $N_v \simeq 3000$ points, which is the actual number of vertices observed in the force tiles from the NESS, this would require 10^6 moves at each configuration, making the simulation prohibitively expensive. Therefore, we used the $\epsilon_{\phi,\sigma}(\mu, N_v)$ computation for smaller sizes ($N_v = 512$ and 1024) to extrapolate to $N_v = 3000$. To perform this extrapolation, we used the data at smaller values of N_v to find a scaling form. We find a reasonably good scaling collapse with the following scaling form

$$\epsilon_{\phi,\sigma}(\mu, N_v) = N_v^3 e_{\phi,\sigma}(\mu), \tag{27}$$

where the function $e_{\phi,\sigma}(\mu)$ is a universal scaling function that is independent of N_v (for large N_v). As shown in Fig. 14, this N_v^3 scaling works well for larger N_v.

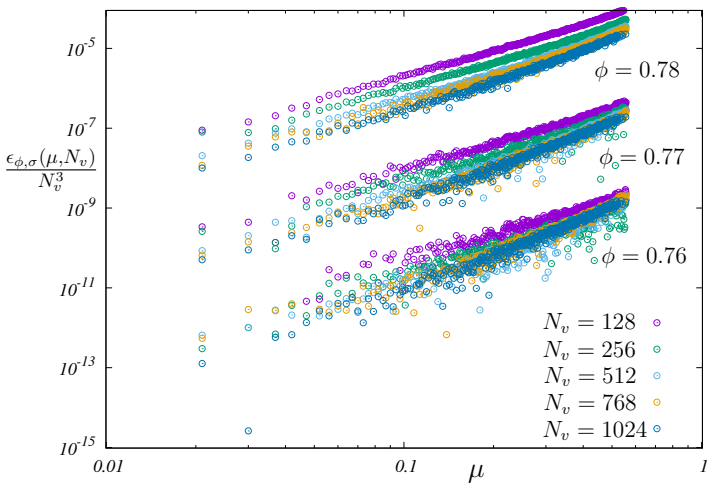

FIG. 14: (Color online) The scaling collapse of $\epsilon_{\phi,\sigma}(\mu, N_v)$ for different values of N_v: $N_v = 128, 256, 512, 768, 1024$, at different values of $\phi = 0.76, 0.77$ and 0.78 with σ_{xy} held fixed at $100\sigma_0$. The curves for different ϕ have been shifted by two decades to aid visualization. We find that a reasonably good scaling collapse emerges with increasing N_v.

The number of MC steps, N_{MC}, ranged from 25000 for $N_v = 1024$ to 50000 for $N_v = 512$. Using these configurations, we computed $\exp\left(-\sum_{i,j} \tilde{V}_{\phi,\sigma}(\vec{s}_i^n - \vec{s}_j^n)\right)$, which we used to calculate $\epsilon_{\phi,\sigma}(\mu, N_v)$ by averaging as follows:

$$\epsilon_{\phi,\sigma}(\mu, N_v) = -\log\left(\sum_{n=1}^{N_{MC}} \exp\left(-\sum_{i,j} \tilde{V}_{\phi,\sigma}(\vec{s}_i^n - \vec{s}_j^n)\right) \Big/ N_{MC}\right). \tag{28}$$

A typical series for $E^n_{\phi,\sigma}(\mu, N_v) = \sum_{i,j} \tilde{V}_{\phi,\sigma}(\vec{s}^n_i - \vec{s}^n_j)$, is shown in Fig. 15 (a) for $\phi = 0.79$, $\sigma_{xy} = 5\sigma_0$, $\mu = 0.33$, and $N_v = 512$. We also demonstrate that the function $\epsilon_{\phi,\sigma}(\mu, N_v)$ asymptotes to an invariant form for $N_{MC} \simeq 20000$ by computing $\frac{\int \epsilon_{\phi,\sigma}(\mu,N_v)d\mu}{\int d\mu}$ for increasing N_{MC} as shown in Fig. 15 (b).

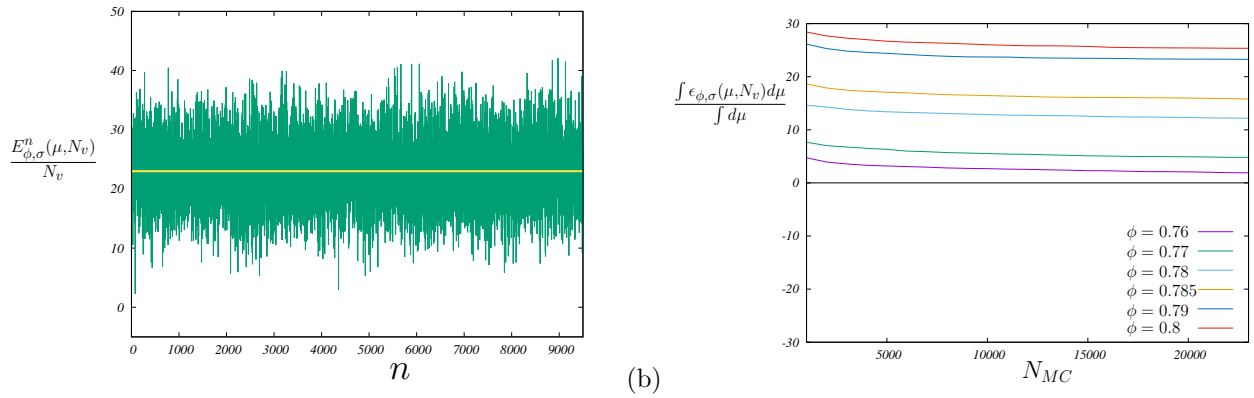

FIG. 15: (Color online) (a) The average "energy" per vertex of each configuration, $\frac{E^n_{\phi,\sigma}(\mu=0.33,N_v)}{N_v}$, at $\phi = 0.79$ and $\sigma = 5\sigma_0$ plotted for different configurations $n = 1, 2...N_{MC}$. (b) The evolution of $\frac{\int \epsilon_{\phi,\sigma}(\mu,N_v)d\mu}{\int d\mu}$ with N_{MC} for different potentials with varying ϕ. We find that this asymptotes to an invariant form for $N_{MC} \simeq 20000$.

* Electronic address: jethomas@brandeis.edu
† Electronic address: kramola@brandeis.edu
‡ Electronic address: asingh@ccny.cuny.edu
§ Electronic address: romain.mari@univ-grenoble-alpes.fr
¶ Electronic address: morris@ccny.cuny.edu
** Electronic address: bulbul@brandeis.edu

[1] F. Boyer, É. Guazzelli, and O. Pouliquen, Physical Review Letters **107**, 188301 (2011).
[2] M. Wyart and M. Cates, Physical review letters **112**, 098302 (2014).
[3] M. E. Cates and M. Wyart, Rheologica Acta **53**, 755 (2014).
[4] A. Singh, J. F. Morris, and M. M. Denn, in *EPJ Web of Conferences*, Vol. 140 (EDP Sciences, 2017) p. 09023.
[5] R. Mari, R. Seto, J. F. Morris, and M. M. Denn, Physical Review E **91**, 052302 (2015).
[6] R. Mari, R. Seto, J. F. Morris, and M. M. Denn, Journal of Rheology **58**, 1693 (2014).
[7] H. M. Laun, J. Non-Newtonian Fluid Mech. **54**, 87 (1994).
[8] R. Mari, R. Seto, J. F. Morris, and M. M. Denn, Proceedings of the National Academy of Sciences **112**, 15326 (2015).
[9] P. A. Cundall and O. D. L. Strack, Geotechnique **29**, 47 (1979).
[10] H. Herrmann and S. Luding, Continuum Mechanics and Thermodynamics **10**, 189 (1998).
[11] A. Singh, V. Magnanimo, K. Saitoh, and S. Luding, New J. Phys **17**, 043028 (2015).
[12] A. Singh, R. Mari, M. M. Denn, and J. F. Morris, Journal of Rheology **62**, 457 (2018).
[13] A. Z. Panagiotopoulos, Molecular Physics **61**, 813 (1987).
[14] S. Yashonath and C. Rao, Molecular Physics **54**, 245 (1985).